Self-assembly of Microcapsules via Colloidal Bond Hybridization and Anisotropy

Chris H.J. Evers, Jurriaan A. Luiken, Peter G. Bolhuis and Willem K. Kegel

Please cite as: Evers *et al. Nature* **534** 364–368 (2016)

Abstract

Particles with directional interactions are promising building blocks for new functional materials and may serve as models for biological structures[1,2,3]. Mutually attractive nanoparticles that are deformable due to flexible surface groups, for example, may spontaneously order themselves into strings, sheets and large vesicles[4,5,6]. Furthermore, anisotropic colloids with attractive patches can self-assemble into open lattices and colloidal equivalents of molecules and micelles[7,8,9]. However, model systems that combine mutual attraction, anisotropy, and deformability have—to the best of our knowledge—not been realized. Here, we synthesize colloidal particles that combine these three characteristics and obtain self-assembled microcapsules. We propose that mutual attraction and deformability induce directional interactions via colloidal bond hybridization. Our particles contain both mutually attractive and repulsive surface groups that are flexible. Analogous to the simplest chemical bond, where two isotropic orbitals hybridize into the molecular orbital of H_2, these flexible groups redistribute upon binding. Via colloidal bond hybridization, isotropic spheres self-assemble into planar monolayers, while anisotropic snowman-like particles self-assemble into hollow monolayer microcapsules. A modest change of the building blocks thus results in a significant leap in the complexity of the self-assembled structures. In other words,

these relatively simple building blocks self-assemble into dramatically more complex structures than similar particles that are isotropic or non-deformable.

For self-assembly of nanoparticles, deformability and mutual attraction have recently been combined by grafting flexible polymers onto the surface of mutually attractive particles. This results in isotropic clusters[10], and self-assembled strings, sheets, and large vesicles[4,5]. For micrometre-sized colloids, on the other hand, coupling mutual attraction and anisotropy leads to *patchy particles*. Attractive domains, or *patches*, have induced self-assembly into open lattices and colloidal equivalents of molecules and micelles[7,8,9]. Here, we combine the three properties mutual attraction, anisotropy and deformability, by synthesizing snowman-like particles that consist of a deformable core and a non-deformable lobe or *protrusion*. In the first part of this letter, mutual attraction is combined with deformability, resulting in anisotropic or *directional* interactions as flexible surface groups redistribute upon binding (Fig. 1e). This process is analogous to bond hybridization in quantum chemistry. When two hydrogen atoms bind and form H_2, for example, the electrons around each atom redistribute, i.e. two isotropic orbitals hybridize into the molecular orbitals of H_2. Similarly, when mutually attractive, deformable particles bind, flexible surface groups redistribute, resulting in directional interactions. We refer to this effect as colloidal bond hybridization. We observe fundamentally new behaviour upon combining colloidal bond hybridization with anisotropy, i.e. for particles that are mutual attractive and deformable as well as anisotropic. These snowman-like particles self-assemble into microcapsules, and form spherical cavities at high particle concentrations. We hypothesize that mutual attraction, anisotropy and deformability are sufficient to stabilize curved structures, and we make this hypothesis more plausible with computer simulations.

We create isotropic as well as anisotropic building blocks that are mutually attractive and deformable. Before discussing the more complex anisotropic particles, we consider the basic principles of colloidal bond hybridization using mutually attractive, isotropic, deformable particles. These poly(styrene-*co*-acrylic acid) spheres are synthesized by copolymerization in water (Fig. 1a–b), and acrylic acid and styrene are incorporated at different stages in the polymerization process[11,12]. Hence, the particles consist of a hydropho-

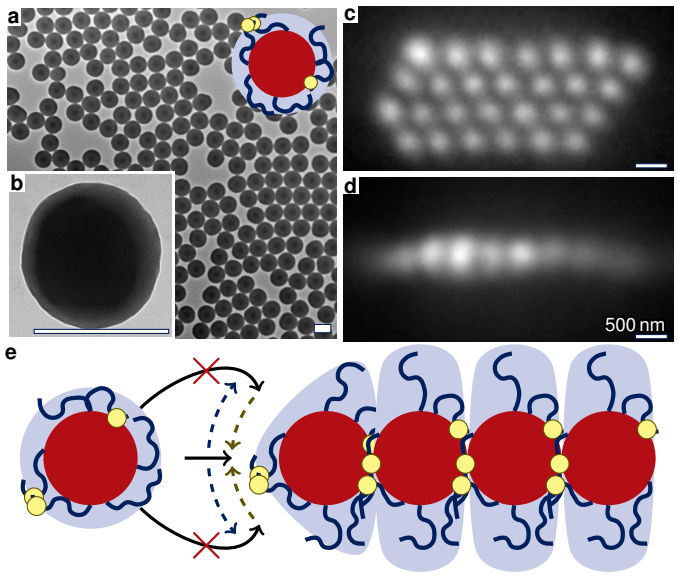

Figure 1: *Self-assembled planar monolayers.* Mutually attractive, isotropic, deformable particles (a–b, transmission electron microscopy) consist of a polystyrene-rich core (red), a deformable poly(acrylic-acid)-rich brush (blue) and mutually attractive moieties (yellow). In water, the particles self-assemble into planar hexagonal monolayers (c–d, top and side view, reflected light microscopy). In colloidal bond hybridization (e), surface groups of deformable particles redistribute upon binding; mutually attractive moieties (yellow) move towards the contact area, while hydrophilic chains (blue) move into the solution.

bic polystyrene-rich core and a hydrophilic poly(acrylic acid)-rich brush. The particles are mutually attractive as hydrophobic polystyrene groups are present both in the interior of the particles as well as in the poly(acrylic acid)-rich brush. Furthermore, dynamic light scattering shows that the poly(acrylic acid)-rich brush can rearrange on the order of 0.1 µm, rendering the particles deformable (Extended Data Fig. 1).

Mutually attractive, isotropic, deformable particles self-assemble into planar monolayers in water (Fig. 1c–d). The monolayer sheets are hexagonally ordered, and move freely in the solution (Supplementary Video 1). We hypothesize that a colloidal equivalent of bond hybridization drives the formation of monolayers. The polymer brush contains hydrophobic styrene groups as well as hydrophilic acrylic acid groups (Fig. 1e yellow and blue). Attrac-

tion between the hydrophobic groups promotes compact structures, while excluded volume effects of the hydrophilic parts favour unbound particles. To accommodate both effects, the polymer brush rearranges upon binding: hydrophobic parts interact in-plane, while hydrophilic parts expand out-of-plane. Consequently, directional interactions are induced and planar monolayers are formed (Fig. 1e).

This segregation process is similar to phase segregation in self-assembly of block copolymers[13]. In our system, however, copolymers are anchored to the surface of µm-sized particles. Consequently, molecular segregation of the polymers induces directional interactions on the colloidal length scale. Our observations are also in line with results for polymer-grafted nanoparticles that are mutually attractive, isotropic and deformable[4,5,6,14]. In our system, however, directional interactions are induced for particles that are two orders of magnitude larger than in previous work. Finally, DNA coated colloids can also form crystalline monolayers[15], but for these particles, a functionalized surface induces directional interactions.

In the remainder of this paper, we combine colloidal bond hybridization with anisotropy, which results in fundamentally new behaviour. Anisotropic building blocks are synthesized by growing a rigid protrusion onto the deformable spheres of Fig. 1 (Extended Data Fig. 2). The second lobe is grown by swelling with additional styrene[16,17,18]. Furthermore, we increase the attraction between the deformable lobes by functionalizing the poly(acrylic acid)-rich brush with hydrophobic groups[19] (Extended Data Fig. 10). Next, the particles are washed by centrifugation, which is a crucial step as we will see later. Finally, we obtain snowman-like particles that consist of a deformable lobe and a non-deformable lobe (Fig. 2a).

These mutually attractive, anisotropic, deformable particles self-assemble into monolayer microcapsules (Fig. 2). The microcapsules can be observed after sintering or freeze drying with scanning electron microscopy (Fig. 2a, Extended Data Fig. 3). Due to the relatively large size of the particles, however, we can even study structures in solution using optical microscopy (Fig. 2g–j). The microcapsules consist of a particle monolayer while the interior is water-filled (Fig. 2c, Supplementary Video 3). Furthermore, most particles align tangentially to the surface of the microcapsules, with the protrusions pointing either slightly inwards or slightly outwards (Fig. 2a–b, Extended Data Fig. 3).

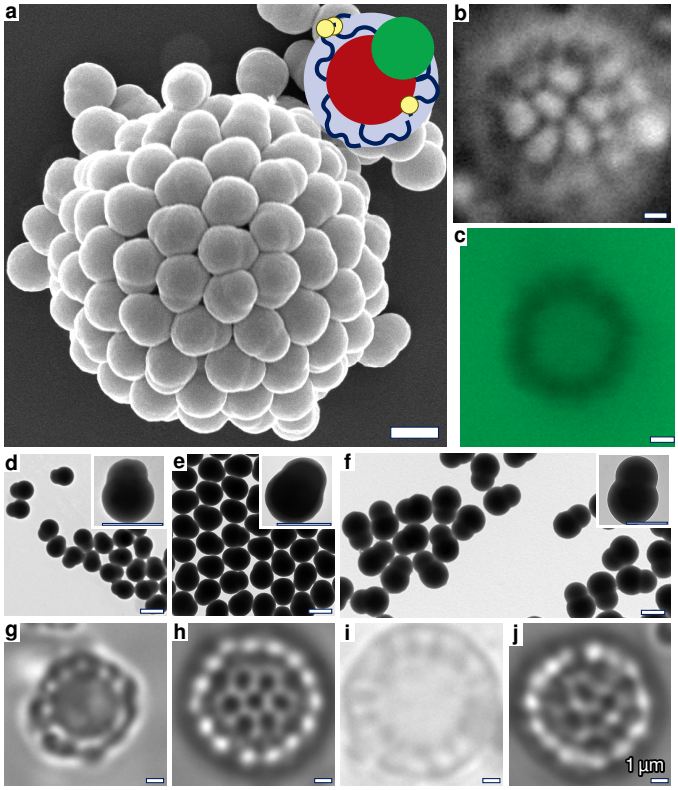

Figure 2: *Self-assembled monolayer microcapsules.* Deformable, anisotropic, mutually attractive particles consist of a core (a, red) with hydrophilic (blue) and hydrophobic (yellow) moieties and a rigid protrusion (green), and self-assemble into microcapsules (a, scanning electron microscopy after sintering). In solution, the particles align tangentially (b, reflected light microscopy), and the microcapsules are water-filled (c, confocal fluorescence microscopy with dyed water phase). Particles are synthesized with large lobes of diameters 445, 540 and 626 nm (d–f, transmission electron microscopy). For each size (g–i, bright field microscopy), and upon functionalization with both fluoresceinamine (g–i) and *tert*-butylamine (j, bright field microscopy), self-assembled microcapsules are found.

For particles with a large lobe of 0.540 µm in diameter, the mean diameter of the microcapsules is 3.7 ± 0.8 µm corresponding to about 10^2 particles per microcapsule. Most particles have six nearest neighbours, but pentagons occur frequently as expected from the Euler characteristic of a sphere (Fig. 2a, Supplementary Video 2). The structure of the microcapsules, however, has no overall icosahedral symmetry. Furthermore, excess styrene is removed before the microcapsules are formed, so unlike colloidosomes—that are formed on emulsion droplets[20]—no template is involved.

By systematically varying the complexity of the particles, we identify that in our system, mutual attraction, anisotropy and deformability are required for self-assembly into microcapsules (Extended Data Fig. 4a–d). First, before functionalization with mutually attractive groups, no microcapsules are found for any of the anisotropic, deformable particles in Fig. 2d–f, showing the importance of mutual attraction. Secondly, for hydrophobically functionalized, deformable, but isotropic spheres, also no microcapsules are observed. Finally, for functionalized, anisotropic, but non-deformable snowman-like particles, no microcapsules are observed either. These three characteristics seem sufficient to induce self-assembly into microcapsules, and are relatively easy to experimentally implement. In contrast, particles with four orthogonally attractive patches, that have previously been predicted to induce self-assembly into microcapsules, have not been experimentally realized yet[21]. Moreover, the self-assembling tendency is robust, as both monolayer microcapsules and planar monolayers are found for snowman-like particles with large lobes of diameters ranging from 445 to 626 nm, and for hydrophobic functionalization with either *tert*-butylamine or fluoresceinamine (Fig. 2d–j, Extended Data Fig. 5).

At high particle concentrations, mutually attractive, anisotropic, deformable particles form curved hollow structures or *cavities*, and these are likely intermediates in the formation of microcapsules. The tendency to form cavities is robust, as similar structures are observed at five different experimental conditions. The first condition is at the edge of an evaporating droplet on a glass slide (Fig. 3a–e). Evaporation of a droplet of particles in water causes a particle flow towards the glass/water/air contact line that is known as the coffee stain effect[22]. For our particles, hemispherical cavities are spontaneously formed in the resulting dense layer near the contact line (Fig. 3b–e, Extended Data Fig. 6a–d). The second condition is for a droplet that is

confined between two parallel glass slides (Fig. 3f–j, Supplementary Video 4). Again, a dense layer is formed at the contact line, but now the layer is two-dimensional with circular cavities. The third condition is at particle volume fractions of ∼0.2, where a highly fluctuating 'cavity phase' is formed (Fig. 3k–n, Supplementary Video 5). In this phase, we observe coexisting regions on the order of 1–10 µm with either high particle concentrations or virtually no particles, i.e. dense curved structures around cavities. Fourthly, upon centrifuging particles in a capillary, cavities are observed in the sediment (Fig. 3q–s and Extended Data Fig. 7a). Finally, upon diluting the sediment, again the formation of circular cavities is observed (Fig. 3t–v, Supplementary Video 6).

At all five conditions, the diameters of the cavities are comparable to the diameters of the microcapsules. Furthermore, by systematically varying the complexity of the building blocks, we conclude that—as for the formation of microcapsules—mutually attraction, anisotropy and deformability all greatly influence the formation of cavities (Extended Data Fig. 4). For isotropic particles, we proposed that mutual attraction and deformability induce the observed self-assembly into planar monolayers by colloidal bond hybridization. Based on the above observations, we hypothesize that adding anisotropy to mutually attractive and deformable colloids induces a shift from planar to curved structures, resulting in microcapsules and cavities.

The formation of microcapsules is a rare event as only 1 in every 10^4 particles ends up in a microcapsule. This can be ascribed to the specific orientation of many particles required for the formation of microcapsules, and the initially weak attractive interactions. The latter becomes apparent as the minimum in the effective pair potential is comparable to the thermal energy, $k_{\mathrm{B}}T$ (Fig. 3p), and particles do not form lasting clusters upon collision (Supplementary Video 5). Furthermore, for particles in such non-lasting clusters, the centre-to-centre distance distribution peaks at a 0.1 µm larger distance than for particles in microcapsules (Fig. 3o). The difference in the centre-to-centre distance can be attributed to the hydrophilic chains with an estimated length of about 0.1 µm. These chains need to move out of the binding site upon bond formation (Fig. 1e).

We propose that both the specific orientation and the formation of lasting bonds are induced by centrifugation with cavities as intermediates. The synthesis contains several centrifugation steps and centrifugation induces the formation of spherical cavities with a similar size and shape as microcapsules (Fig. 3q–s). Centrifugation thus aligns the particles in a specific

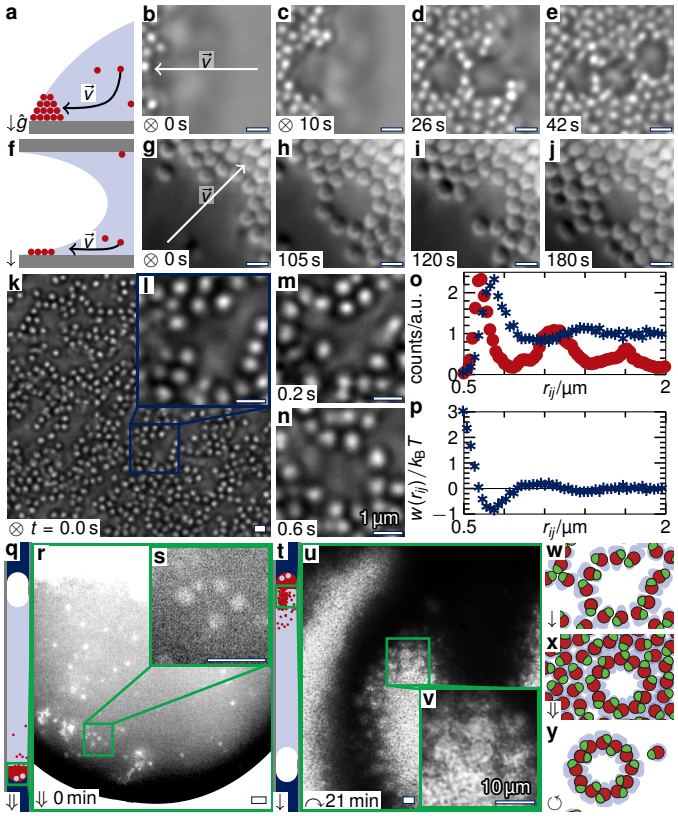

Figure 3: *Cavity formation upon densification.* Cavities are observed at the edge of an evaporating droplet (a–e, multilayer, f–j, monolayer) in a *cavity phase* (k–n), after centrifugation in a thin cell (q–s, bright regions), and upon turning the cell upside down (t–v). The histograms of the interparticle distance, r_{ij} (o) peak at 0.72 µm (cavity phase, blue), and at 0.62 µm (microcapsules, red), and the effective pair potential, $w(r_{ij})$ (p) has a minimum of $-0.8\,k_{\mathrm{B}}T$. Particles form a cavity phase upon densification (w), and are pushed into close contact upon centrifugation (x). We propose that after redispersion (y), particles that surrounded cavities are found as microcapsules. The arrows indicate the flow, $\vec{v}$, and the gravitational field $\hat{g}$.

microcapsule-like orientation. Furthermore, upon centrifugation, particles are pushed close together. This could push the hydrophilic chains out of the binding side, and induce the formation of irreversible bonds that arise from van der Waals forces between the colloids at close proximity. While we have no direct, real-space proof of the formation mechanism, microcapsules could be formed as follows: first, particles form a dense sediment with cavities (Fig. 3w); next, centrifugation pushes particles closer together and irreversible bonds are formed (Fig. 3x); finally, after shaking, particles that surrounded cavities are found as microcapsules (Fig. 3y).

We test the key hypothesis that combining colloidal bond hybridization with anisotropy can stabilize curved monolayers using Monte Carlo simulations. First, we develop a simple model for mutually attractive, isotropic, deformable particles. Next, we extend this model with anisotropy.

Mutually attractive, isotropic, deformable particles are modelled as central spheres with f satellite spheres each (Fig. 4b). The size ratio between the central and the satellite spheres is q, and the latter are penetrable hard spheres that model the flexible surface groups. Penetrable hard spheres can interpenetrate other satellite spheres, but have excluded volume interactions with the central spheres. Mutual attraction is captured by a square well interaction between central spheres, and deformability is incorporated as the satellite spheres can freely move over the surface of the central sphere.

To verify if colloidal bond hybridization can induce directional interactions, i.e. if rearrangement of surface groups can stabilize monolayers, we start Monte Carlo simulations in a hexagonal planar configuration. Different morphologies are observed upon varying the size and the number of satellite spheres (Extended Data Fig. 8b,i–k). These two variables can be combined in the covered surface fraction, $Q = \frac{fq^2}{4(1+q)^2}$. Upon plotting the average number of bonds, $\langle N_\mathrm{b} \rangle$, as a function of Q, all data collapse onto a single curve (Fig. 4a). Furthermore, the transitions between different morphologies occur at well defined Q-values showing that the covered surface fraction dictates the morphology (Fig. 4a, Extended Data Fig. 8b). If the covered surface fraction is small, the particles reorganize into compact aggregates with many bonds to maximize the attractive interaction between the central spheres (Fig. 4c). Upon increasing the size or number of satellite spheres, however, they redistribute out-of-plane and mechanically stable bilayers and monolay-

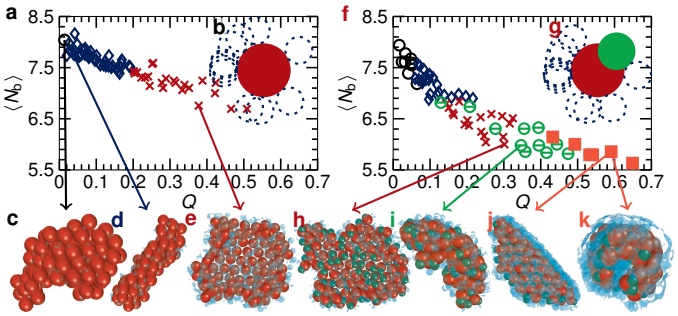

Figure 4: *Monte Carlo simulations.* b) Deformable spheres are modelled as attractive spheres (red) with f mobile penetrable hard spheres (blue). a) The average number of bonds, $\langle N_\mathrm{b} \rangle$ decreases with the covered surface fraction Q, resulting in compact clusters (c, ○), bilayers (d, ◇) and monolayers (e, ×). g) Snowman-like particles are modelled as deformable spheres with a rigid protrusion (green). f) Adding a protrusion induces a shift from flat monolayers (h, ×) to curved monolayers with in-plane protrusions (i, ⊖) and out-of-plane protrusions (j–k, ■) at high Q-values.

ers are observed (Fig. 4d–e). Colloidal bond hybridization can thus induce directional interactions and stabilize monolayers for isotropic particles, which agrees well with the results in Fig. 1.

Starting with unbound particles (Extended Data Fig. 8a,c–h), we qualitatively reproduce simulation results that have been obtained using a more detailed model with tethered chains[4]. Hence, we conclude that, albeit simple, our model captures the main ingredients that induce directional interactions: mutual attraction and deformability. As our model does not contain any molecular details, we expect this behaviour to be generic. This expectation is in line with experimental systems of polymer-grafted nanoparticles where both mutual attraction and deformability can be identified and directional interactions are induced[4,5].

We model mutually attractive, anisotropic, deformable particles by adding a rigid sphere to the deformable sphere (Fig. 4g, Extended Data Fig. 9). The rigid sphere models the polystyrene protrusion in the most primitive way, and its hydrophobicity is captured by a short-ranged attraction with other rigid and central spheres. Similarly as for isotropic particles, the values for the average number of bonds collapse on a single curve as a function of the covered surface fraction (Fig. 4f, Eq. 11), and planar monolayers are stable at mod-

erate values for the covered surface fraction (Fig. 4h). Upon increasing the size and the number of satellite spheres further, however, curved monolayers with protrusions pointing just out-of-plane (Fig. 4i) are observed, while for large and many satellite spheres, all protrusions point inwards (Fig. 4j–k).

We conclude that, as hypothesized, 1) colloidal bond hybridization can stabilize monolayers, and 2) anisotropy induces a shift from planar to curved structures. Furthermore, hemispherical monolayers with in-plane protrusions (Fig. 4i, Supplementary Video 7) resemble segments of the experimentally observed microcapsules.

In this paper, we combined mutual attraction, anisotropy and deformability in colloidal model particles. On the one hand, mutual attraction and deformability cause surface groups to rearrange upon binding, which is a colloidal equivalent of bond hybridization; on the other hand, anisotropy induces curvature. These three characteristics are most likely sufficient to induce self-assembly into microcapsules, a process that—to the best of our knowledge—had not been realized before in a colloidal model system. We note that, while details are different, in the building blocks of viruses, mutual attraction, deformability and anisotropy can also be identified[23,24,25], suggesting that these characteristics could be important in the assembly of virus microcapsules as well. The mechanism we find is fundamentally different from previous work where directional interactions are induced by rigid patches[7,8,9], structural rearrangements upon changing the solvent[26], or electric fields[27]. Quantification of attraction strength, anisotropy, number of particle lobes and deformability lead to a large parameter space that remains to be systematically explored. Additionally, more theoretical work is needed to predict self-assembled structures from these properties, for which work of Asai *et al.* could be extended[14]. Independently controlling these properties, however, seems impossible for proteins; colloidal particles, on the other hand, are promising building blocks to address this challenge.

References

1. Zhang, Z. & Glotzer, S. C. Self-Assembly of Patchy Particles. Nano Lett. **4**, 1407–1413 (2004). URL `http://dx.doi.org/10.1021/nl0493500`.

2. Glotzer, S. C. & Solomon, M. J. Anisotropy of building blocks and their assembly into complex structures. Nature Mater. **6**, 557–562 (2007). URL http://dx.doi.org/10.1038/nmat1949.

3. Yi, G.-R., Pine, D. J. & Sacanna, S. Recent progress on patchy colloids and their self-assembly. J. Phys. Condens. Matter **25**, 193101 (2013). URL http://dx.doi.org/10.1088/0953-8984/25/19/193101.

4. Akcora, P. *et al.* Anisotropic self-assembly of spherical polymer-grafted nanoparticles. Nature Mater. **8**, 354–359 (2009). URL http://dx.doi.org/10.1038/nmat2404.

5. Nikolic, M. S. *et al.* Micelle and vesicle formation of amphiphilic nanopartieles. Angew. Chem. Int. Ed. **48**, 2752–2754 (2009). URL http://dx.doi.org/10.1002/anie.200805158.

6. Luiken, J. A. & Bolhuis, P. G. Anisotropic aggregation in a simple model of isotropically polymer-coated nanoparticles. Phys. Rev. E **88**, 012303 (2013). URL http://dx.doi.org/10.1103/PhysRevE.88.012303.

7. Chen, Q., Bae, S. C. & Granick, S. Directed self-assembly of a colloidal kagome lattice. Nature **469**, 381–384 (2011). URL http://dx.doi.org/10.1038/nature09713.

8. Wang, Y. *et al.* Colloids with valence and specific directional bonding. Nature **491**, 51–55 (2012). URL http://dx.doi.org/10.1038/nature11564.

9. Kraft, D. J. *et al.* Surface roughness directed self-assembly of patchy particles into colloidal micelles. Proc. Natl. Acad. Sci. **109**, 10787–10792 (2012). URL http://dx.doi.org/10.1073/pnas.1116820109.

10. Larson-Smith, K. & Pozzo, D. C. Scalable synthesis of self-assembling nanoparticle clusters based on controlled steric interactions. Soft Matter **7**, 5339–5347 (2011). URL http://dx.doi.org/10.1039/C0SM01497D.

11. Wang, P. H. & Pan, C.-Y. Preparation of styrene/acrylic acid copolymer microspheres: polymerization mechanism and carboxyl group distribution. Colloid & Polym. Science **280**, 152–159 (2002). URL http://dx.doi.org/10.1007/s003960100588.

12. Hu, X., Liu, H., Ge, X., Yang, S. & Ge, X. Preparation of Submicron-sized Snowman-like Polystyrene Particles via Radiation-induced Seeded Emulsion Polymerization. Chem. Lett. **38**, 854–855 (2009). URL http://dx.doi.org/10.1246/cl.2009.854.

13. Bates, F. S. Polymer-Polymer Phase Behavior. Science **251**, 898–905 (1991). URL http://dx.doi.org/10.1126/science.251.4996.898.

14. Asai, M., Cacciuto, A. & Kumar, S. K. Quantitative analogy between polymer-grafted nanoparticles and patchy particles. Soft matter **11**, 793–797 (2015). URL http://dx.doi.org/10.1039/C4SM02295E.

15. Geerts, N. & Eiser, E. Flying colloidal carpets. Soft Matter **6**, 664–669 (2010). URL http://dx.doi.org/10.1039/B917846E.

16. Sheu, H. R., El-Aasser, M. S. & Vanderhoff, J. W. Uniform nonspherical latex particles as model interpenetrating polymer networks. J. Polym. Science Part A: Polym. Chem. **28**, 653–667 (1990). URL http://dx.doi.org/10.1002/pola.1990.080280315.

17. Mock, E. B., De Bruyn, H., Hawkett, B. S., Gilbert, R. G. & Zukoski, C. F. Synthesis of Anisotropic Nanoparticles by Seeded Emulsion Polymerization. Langmuir **22**, 4037–4043 (2006). URL http://dx.doi.org/10.1021/la060003a.

18. Kraft, D. J., Groenewold, J. & Kegel, W. K. Colloidal molecules with well-controlled bond angles. Soft Matter **5**, 3823 (2009). URL http://dx.doi.org/10.1039/b910593j.

19. Marchand-Brynaert, J., Deldime, M., Dupont, I., Dewez, J.-L. & Schneider, Y.-J. Surface Functionalization of Poly(ethylene terephthalate) Film and Membrane by Controlled Wet Chemistry: Chemical Characterization of Carboxylated Surfaces. J. Colloid Interface Science **173**, 236–244 (1995). URL http://dx.doi.org/10.1006/jcis.1995.1319.

20. Dinsmore, A. D. *et al.* Colloidosomes: selectively permeable capsules composed of colloidal particles. Science **298**, 1006–1009 (2002). URL http://dx.doi.org/10.1126/science.1074868.

21. Chen, T., Zhang, Z. & Glotzer, S. C. Simulation Studies of the Self-Assembly of Cone-Shaped Particles. Langmuir **23**, 6598–6605 (2007). URL http://pubs.acs.org/doi/abs/10.1021/la063755d.

22. Deegan, R. D. *et al.* Capillary flow as the cause of ring stains from dried liquid drops. Nature **389**, 827–829 (1997). URL http://dx.doi.org/10.1038/39827.

23. Berg, J. M., Tymoczko, J. L. & Stryer, L. *Biochemistry* (W. H. Freeman and Company: New York, 2002).

24. Tompa, P. & Fuxreiter, M. Fuzzy complexes: polymorphism and structural disorder in protein-protein interactions. Trends Biochem. Sci. **33**, 2–8 (2008). URL http://dx.doi.org/10.1016/j.tibs.2007.10.003.

25. Freund, S. M. V., Johnson, C. M., Jaulent, A. M. & Ferguson, N. Moving towards High-Resolution Descriptions of the Molecular Interactions and Structural Rearrangements of the Human Hepatitis B Core Protein. J. Mol. Biol. **384**, 1301–1313 (2008). URL http://dx.doi.org/10.1016/j.jmb.2008.10.020.

26. Groschel, A. H. *et al.* Guided hierarchical co-assembly of soft patchy nanoparticles. Nature **503**, 247–251 (2013). URL http://dx.doi.org/10.1038/nature12610.

27. Crassous, J. J. *et al.* Field-induced assembly of colloidal ellipsoids into well-defined microtubules. Nature Commun. **5**, 5516 (2014). URL http://dx.doi.org/10.1038/ncomms6516.

Supplementary Information is available in the online version of the paper.

Acknowledgements The authors thank Bas van Ravensteijn for providing non-deformable, fluorescein functionalized snowman-like particles, Sonja Castillo for taking the scanning electron microscopy images and Hans Meeldijk and Chris Schneijdenberg for help with freeze drying and transmission electron microscopy. This work is part of the research programmes VICI 700.58.442 and TOP-GO 700.10.355, which are financed by the Netherlands Organization for Scientific Research (NWO). Alfons van Blaaderen and Marjolein Dijkstra are thanked for useful discussion, and Mathijs de Jong is thanked for critically reading the manuscript.

Author Contributions All authors designed the research; C.E. synthesised the particles and analysed the self-assembled structures; J.L. performed and analysed the Monte Carlo simulations. W.K. and P.B. supervised the project. All authors discussed the results and implications and wrote the paper.

Author Information Reprints and permissions information is available at www.nature.com/reprints. The authors declare no competing financial interests. Correspondence and requests for materials should be addressed to C.E. (c.h.j.evers@uu.nl) or W.K. (w.k.kegel@uu.nl).

Methods

Chemicals Unless stated otherwise, the following chemicals were used as received: acrylic acid (AA, 99%), aluminum oxide (Al_2O_3, puriss., ≥98%), *tert*-butylamine (tBA, ≥99.5%), divinyl benzene (DVB, 55%, mixture of isomers), fluorescein sodium salt (Fl, F6377), fluoresceinamine (FlA, mixture of isomers, ≥75%), *N*-(3-Dimethylaminopropyl)-*N*'-ethylcarbodiimide hydrochloride (EDC, purum, ≥98.0%), 2-(N-Morpholino)ethanesulfonic acid (MES,≥99%), sodium phosphate dibasic (Na_2HPO_4, BioXtra, ≥99%), sodium phosphate monobasic dihydrate ($NaH_2PO_4 \cdot 2H_2O$, BioUltra, ≥99%), and styrene (St, ReagentPlus, ≥99%), were obtained from Sigma-Aldrich or its subsidiaries; 2,2'-azobis(2-methylpropionitrile) (AIBN, 98%), potassium chloride (KCl, p.a.), and potassium persulfate (KPS, reagent ACS, 99+%) were obtained from Acros Organics; hydroquinone (puriss, ≥99.5%) was obtained from Riedel-de Haën; glycerol (Ph Eur) was obtained from Bufa; ethanol (100%) was obtained from Interchema; potassium hydroxide (KOH) was obtained from Emsure; hydrochloric acid (HCl, 37%) was obtained from Merck; and Millipore water (MQ) was obtained with a Synergy water purification system.

Synthesis The synthesis is outlined in Extended Data Fig. 2a and involved (i) emulsifier-free polymerization of cross-linked poly(styrene-*co*-acrylic acid) (CPSAA) spheres, (ii) protrusion formation by swelling with styrene, heating and polymerizing and (iii) covalently linking hydrophobic moieties to the carboxylic groups.

Cross-linked poly(styrene-*co*-acrylic acid) spheres of 0.530 ± 0.014 µm in diameter are prepared by emulsifier-free polymerization of styrene, acrylic acid and divinyl benzene based on Wang and Pang and Hu *et al.*[11,12]. 90 ml MQ, 11 ml St passed over an Al_2O_3 column, 761 µl freshly opened AA, and 55 µl DVB were added to a 250 ml three-neck round-bottom flask. The flask was constantly and vigorously stirred with a glass stirrer under nitrogen flow. Quantitatively, 0.05 g KPS was dissolved as an initiator and added to the flask with 10 ml MQ. After 15 minutes, the nitrogen inlet was raised above the liquid level, and after 15 more minutes, the flask was immersed in a 70 °C oil bath to start the polymerization. After 20 hours, a milky-white dispersion was obtained. Excess reactants were removed by centrifugation (Beckman Coulter Allegra X-12R). Upon centrifugation, particles settle at the bottom of the sample, while unreacted chemicals were in the so-called

supernatant. Three times, the dispersion was washed by centrifugation at $2.1 \times 10^3\, g$ and the supernatant was replaced by MQ.

Cross-linked polystyrene (CPS) spheres are prepared in a similar method. For these particles, 225 ml MQ, 23.5 ml St and 0.7 ml DVB were added to a 500 ml one-neck round-bottom flask. The flask was constantly and vigorously stirred with a PTFE coated stir bar, immersed in an 80 °C oil bath, and 0.78 g KPS in 37.5 ml MQ was added. After 24 h a milky-white dispersion was obtained, which was washed three times by centrifugation and redispersed in MQ.

To form a protrusion, the CPSAA spheres were swollen with St, heated and polymerized, in line with Sheu *et al.*, Mock *et al.* and Kraft *et al.*[16,17,18]. In a typical experiment, the solid mass fraction—as determined by drying—was brought to 3–6% with MQ. About 5 ml dispersion was magnetically stirred with a PTFE coated stir bar in a glass tube. Styrene was added with a swelling ratio $S = m_{\mathrm{St}}/m_{\mathrm{s}} = 3$–$7$ with m_{St} and m_{s} being the mass of added St, and the solid mass in the dispersion. After one to two days stirring, the tube was immersed in an 80 °C oil bath for two hours under continuous stirring to form a styrene protrusion. Next, 500 µl of an aqueous hydroquinone solution (45 mg/50 ml) and 5 mg AIBN in 250 µl St were added, and the tube was immersed in the 80 °C oil bath for 24 h to polymerize the protrusion. Finally, a milky white dispersion was obtained. A mm-sized solid white aggregate was often found, which could easily be removed.

Hydrophobic moieties are covalently linked to carbodiimide activated carboxylic groups on CPSAA particles, a method adapted from Marchand-Brynaert *et al.*[19]. In a typical synthesis, a 0.1 M MES buffer (1.95 g in 100 ml MQ), and a 0.2 M phosphate buffer (6.72 g Na_2HPO_4 and 0.41 g $NaH_2PO_4 \cdot 2H_2O$ in 250 ml MQ) were prepared. 2.5 ml dispersion was centrifuged, and the supernatant was replaced by an EDC/MES solution (45 mg EDC quantitatively added with 40 ml MES buffer) to activate the AA groups. The dispersion was tumbled at 60 rpm for one hour, and washed by centrifugation at $2.1 \times 10^3\, g$ with MES buffer and twice with MQ. The dispersion was again centrifuged, and after removal of the supernatant, 0.028 mmol FlA or tBA was quantitatively added with 30 ml phosphate buffer to covalently bind FlA or tBA to the activated AA groups. The tube was wrapped in aluminium foil, and after tumbling at 60 rpm overnight, the dispersion was washed three times with phosphate buffer, once with MES solution, and five times with MQ. Finally, a milky white dispersion was obtained. Covalent linkage of fluoresceinamine was verified by varying the flu-

oresceinamine coupling method and studying the resulting washed particles using fluorescence microscopy (Extended Data Fig. 10). The preparation of non-deformable, fluoresceinamine functionalized snowman-like particles was previously described by van Ravensteijn *et al.*[28].

Transmission Electron Microscopy Analysis Transmission electron microscopy (TEM) images were taken with a Philips TECNAI 10 at 100 kV and 16-bit. Samples were prepared by drying a diluted dispersion droplet on a polymer coated copper grid under illumination with a heat lamp. Image levels were linearly rescaled using ImageMagick, so that 99.9% of all values were between the lower and upper level thresholds.

Fig. 1a was obtained at 9.7 nm/px and 1b at 0.95 nm/px. Fig. 2d–e were obtained at 3.5 nm/px, 2f at 6.8 nm/px, and the insets in 2d–f at 0.95 nm/px. Extended Data Fig. 2b and 2d were obtained at 4.9 nm/px, and 2c and 2e at 0.95 nm/px. Extended Data Fig. 5a–d were obtained at 0.9 nm/px.

Particle sizes were measured using Gaussian ring transformations in Wolfram Mathematica 10. For spherical particles, a gradient transform was computed using discrete derivatives of a Gaussian. Circles were detected by iteratively convolving with Gaussian rings, and finding the maxima.

Scanning Electron Microscopy By freeze-drying or sintering, self-assembled structures could be preserved upon drying and studied using scanning electron microscopy. For freeze-drying, 1 µl dispersion was brought on a polymer coated copper grid. The grid was vitrified in liquid nitrogen and mounted on a cryotransfer unit which was brought under vacuum. Temperature was increased to -90 °C at 5 °C/min and kept constant for about six hours to allow the water to sublimate.

For sintering, the sample was heated above the glass transition temperature of polystyrene at about 100 °C. First, the dispersion was centrifuged and after redispersion in 1:1 glycerol:water, immersed in an 105 °C oil bath for 30 minutes. The dispersion was washed three times by centrifugation with MQ and 1 µl was brought on a polymer coated copper grid. After drying, the sample was coated with a $\sim$ 6 nm platinum layer.

Both samples were studied with a FEI XL30 FEG operated at 5-10 kV, and images were obtained at 8-bit. Image levels were linearly rescaled using ImageMagick, from the value of the pixel with the lowest intensity to the

brightest pixel. Fig. 2a was obtained at 6.5 nm/px. Extended Data Fig. 3c was obtained at 3.5 nm/px, d at 1.9 nm/px, e at 3.5 nm/px, h at 11 nm/px, i at 6.9 nm/px and j at 11 nm/px.

Optical Microscopy Bright field, fluorescence and reflected light microscopy images were captured with a Nikon Ti-E Inverted Microscope unless stated otherwise. The Nikon Ti-E was operated with a Nikon TIRF $100\times/1.49$ objective, intermediate magnification of $1.5\times$, and a Hamamatsu ORCA Flash camera at 16-bit. For reflected light microscopy, a Nikon Intensilight C-HGFl light source was used with a Nikon D-FLE filter block. For fluorescence microscopy, the same light source was used with a Semrock FITC-3540C filter block. The bright field microscopy images in Fig. 3k–n were obtained with a Nikon Ti-U inverted Microscope with a Nikon Plan Apo VC $100\times/1.40$ objective, intermediate magnification of $1.5\times$, and a Lumenera Infinity X camera at 8-bit. The bright field microscopy images in Fig. 3r–s,u–v, Extended Data Fig. 4i–v and Extended Data Fig. 7 were obtained with a Nikon Eclipse LV100POL microscope with its focal plane parallel to the gravitational field, a Nikon Plan Fluor ELWD $40\times/0.6$ objective, and a QImaging MicroPublisher 5.0 camera at 8-bit. Finally, confocal microscopy images were captured with a Nikon TE2000-U, with a Nikon Plan Apo $100\times/1.40$ objective and a 488 nm laser and a 590 nm detector at 12-bit. For images obtained with the TiE and the TE2000-U, bitmaps were extracted from the microscopy files using bfconvert 5.1.7 (Open Microscopy Environment). Furthermore, image levels were linearly rescaled using ImageMagick.

Fig. 1c–d were obtained with the TiE in reflected light mode at 40 nm/px and image levels were linearly rescaled from the value of the darkest to the brightest pixel. Fig. 2b was obtained with the TiE in reflected light mode at 43 nm/px, and levels were linearly rescaled from the value of the darkest pixel to the brightest pixel. Fig. 2c was obtained with the TE2000-U in confocal fluorescence mode at 35.72 nm/px, and levels were linearly rescaled from zero to the value of the brightest pixel. Fluorescein sodium salt was added to the water phase, and the image was false coloured in green. Fig. 2g–j were obtained with the TiE in bright field mode at 43 nm/px, and levels were linearly rescaled from zero to the value of the brightest pixel. Fig. 3b–e were obtained with the TiE in bright field mode at 40 nm/px, and levels were linearly rescaled from zero to the value of the brightest pixel. Fig. 3g–j were obtained with the TiE in reflected light mode at 43 nm/px, and levels

were linearly rescaled from the value of the darkest pixel to the brightest pixel. Fig. 3k–n were obtained with the TiU in reflect light mode at 29 nm/px, and levels were linearly rescaled from the value of the darkest pixel to the brightest pixel. Fig. 3r–s,u–v were obtained with the LV100POL at 86 nm/px. For s and v, levels were linearly rescaled from the value of the darkest pixel to the brightest pixel, and these thresholds were also used for r and u. Extended Data Fig. 2f–g were obtained with the TiE in fluorescence mode at 43 nm/px, and levels were linearly rescaled from zero to the value of the brightest pixel. Extended Data Fig. 4a was obtained with the TiE in bright field mode at 43 nm/px, and levels were linearly rescaled from zero to the value of the brightest pixel. Extended Data Fig. 4e–h were obtained with the TiE in bright field mode at 40 nm/px, and levels were linearly rescaled from zero to the value of the brightest pixel. Extended Data Fig. 4i–v were obtained with the LV100POL at 86 nm/px. For m–o and t–v, levels were linearly rescaled from the value of the darkest pixel to the brightest pixel, and these thresholds were also used for i–k and q–s. For l and p, levels were linearly rescaled from zero to the value of the brightest pixel. Extended Data Fig. 5e–h were obtained with the TiE in bright field mode at 43 nm/px, and levels were linearly rescaled from zero to the value of the brightest pixel. The images in Extended Data Fig. 6 were obtained with the TiE in bright field mode at 40 nm/px, and levels were linearly rescaled from zero to the value of the brightest pixel. The images in Extended Data Fig. 7 were obtained with the LV100POL at 86 nm/px. Image levels were linearly rescaled using the thresholds from Fig. 3s and Extended Data Fig. 4m–o. Extended Data Fig. 10a–d were obtained with the TiE in fluorescence mode at 43 nm/px, levels were linearly rescaled from zero to the value of the brightest pixel, and the images were false coloured in green.

Typically, a sample was prepared by bringing 0.5–2 µl dispersion between a microscope slide (Menzel-Gläser), and a #1.5 cover slip (Menzel-Gläser) with two #0 cover glasses (VWR) as spacers. Before use, the slides were cleaned with MQ, ethanol and Kimtech precision wipes, and cells were sealed with glue (Norland NOA81, after UV curing) or scotch tape. Evaporating droplets between two glass slides (Fig. 3f–j) were studied in cells as described above, but without sealing the sides of the cell. Evaporating droplets on a glass slide (Fig. 3a–e, Extended Data Fig. 4e–h and Extended Data Fig. 6), on the other hand, were studied by bringing 0.5 µl dispersion on a cleaned #1.5 cover slip (Menzel-Gläser). Droplets evaporated spontaneously and for each dispersion, four times (twice for non-deformable particles) a time series,

was obtained of 89 µm of the contact line (Extended Data Fig. 6). High concentration samples (Fig. 3k–n, Supplementary Video 5) were studied after sedimentation in the gravitational field in a similar cell as described above. Thin cells as in Fig. 3q–v and Extended Data Fig. 4i–v and Extended Data Fig. 7 were prepared in a capillary and sealed with glue, while preventing contact between uncured glue and the dispersion. A $0.020 \times 0.200 \times 50$ mm^3 capillary (VitroCom 5002-050, Kimtech cleaned) was filled half with dispersion. Next, the capillary was pressed on a microscopy slide (Menzel-Gläser) with tweezers and a foam cushion, and nitrogen gas was blown from the filling side to push the dispersion to the middle of the tube. While blowing, the other side was sealed with a glue droplet (Norrland NOA81) to prevent the dispersion from flowing back. Finally, the other side was sealed with glue, the glue was cured with UV light, and the cells were centrifuged in centrifuge tubes (VWR SuperClear).

Interparticle distance distributions were obtained by analysing reflected light microscopy time series with Mathematica. For each frame, the gradient transform was computed using discrete derivatives of a Gaussian, and the gradients were circle transformed by convolving with a circle. The original image was multiplied pixel per pixel with the circle transform, and the local maximums were identified as particles. The histogram for particles in the cavity phase (Fig. 3o, blue) was normalized with a fitted function through the distribution of 10^7 distances between random points on a plane with the same size as the microscopy images, and the resulting histogram was scaled to 1 at large inter-particle distances. The effective pair potential (Fig. 3p) was calculated using $w(r_{ij})/k_BT = -\ln g(r_{ij})$, where $g(r_{ij})$ is the measured interparticle distance distribution. The histogram for particles in a microcapsule (Fig. 3p, red) was scaled so the maximum has the same height as the maximum of the cavity phase histogram.

The number of particles per microcapsule was estimated from the first peak in the interparticle distance distribution of a microcapsule, $r^*_{ij} = 0.62$ µm, by assuming a hexagonal orientation, and a spherical microcapsule surface,

$$N_{\text{part}} = \frac{A_{\text{tot}}}{A_{\text{part}}} = \frac{4\pi R_{\text{m}}^2}{\frac{\sqrt{3}}{2} {r^*_{ij}}^2} \tag{1}$$

with A_{tot} the surface area of a microcapsule, A_{part} the surface area per particle and R_{m} the radius of the microcapsules. For particles with a large lobe with diameter 0.540 µm, the radii of 30 microcapsules, $R_{\text{m}} = 1.9 \pm 0.4$ µm, was

determined similarly as for transmission electron microscopy. Finally, the estimated number of particles per microcapsule was $N_{\mathrm{part}} = 10^2$.

Dynamic Light Scattering Cross-linked poly(styrene-*co*-acrylic acid) spheres were added to 1 mM KOH, and using a Malvern Zetasizer Nano ZS, equipped with an MPT-2 autotitrator, pH was stepwise decreased from 9.8 to 3.4 by adding 1 mM HCl. Cumulant analysis gave the apparent size and polydispersity index. The influence of electrostatic interactions was studied by replacing the solvents with 1 mM KOH / 9 mM KCl and 1 mM HCl / 9 mM KCl. The influence of the carboxylic acid groups was studied by using cross-linked polystyrene spheres instead of CPSAA spheres.

Simulation model We model the colloids as hard-spheres of diameter σ. The attractive forces between particles, due to e.g. van der Waals interactions and the hydrophobic (polystyrene) component of the brush, is captured using a square well potential:

$$U_{\mathrm{cc}}(R) = \begin{cases} \infty & R \leq \sigma, \\ -\varepsilon_{\mathrm{c}} & \sigma < R \leq \sigma + \Delta, \\ 0 & R > \sigma + \Delta, \end{cases} \tag{2}$$

where Δ is the width of the well and R is the centre-centre distance between the colloids. We then model the grafted acrylic acid polymers as penetrable hard spheres (PHS) or satellite spheres with diameter $q\sigma$ [29], which can move freely across the surface at a fixed distance $(\sigma + q\sigma)/2$, thereby allowing the brush to adapt its configuration to the environment. The PHS particles are free to overlap each other, i.e. $U_{\mathrm{PHS-PHS}} = 0$, but have a hard-sphere interaction with the colloids:

$$U_{\mathrm{PHS-c}}(r) = \begin{cases} \infty & r \leq (\sigma + q\sigma)/2, \\ 0 & r > (\sigma + q\sigma)/2, \end{cases} \tag{3}$$

where r is the centre-centre distance between the colloid and polymer.

To obtain snowman-like particles, we attach a protrusion to each colloid, modelled here as a hard-sphere with radius r_{p}, with its centre located at the colloid surface. The protrusion hydrophobicity is captured by a weak square-well attraction between protrusions with strength $U_{\mathrm{pp}} = -\varepsilon_{\mathrm{p}}$ over the range $2r_{\mathrm{p}} < R \leq 2r_{\mathrm{p}} + \Delta$. The colloids and protrusions interact through a square-well potential with depth $U_{\mathrm{cp}} = -\sqrt{\varepsilon_{\mathrm{c}}\varepsilon_{\mathrm{p}}}$, i.e. the geometric mean

of the interaction strengths, over the range $\sigma/2 + r_\mathrm{p} < R \leq \sigma/2 + r_\mathrm{p} + \Delta$. Lastly, the protrusions have a hard-sphere interaction with the polymers:

$$U_{\mathrm{PHS-p}}(r) = \begin{cases} \infty & r \leq r_\mathrm{p} + q\sigma/2, \\ 0 & r > r_\mathrm{p} + q\sigma/2. \end{cases} \tag{4}$$

Given a system containing N particles at positions $\mathbf{R}^N$, each grafted with f polymers at positions $\mathbf{r}^f$, the total energy for the system is then given by

$$\begin{aligned} U(\mathbf{R}^N, \mathbf{r}^{fN}) = \sum_{i \neq j}^{N} \Big[& U_\mathrm{cc}(\vec{R}_{ij}) + U_\mathrm{cp}([\vec{R}_i + \vec{u}_i] - \vec{R}_j) \\ & + U_\mathrm{cp}(\vec{R}_i - [\vec{R}_j + \vec{u}_j]) + U_\mathrm{pp}([\vec{R}_i + \vec{u}_i] - [\vec{R}_j + \vec{u}_j]) \Big] \\ & + \sum_{i,j}^{N} \sum_{k}^{f} \Big[U_{\mathrm{PHS-c}}(\vec{r}_{i,k} - \vec{R}_j) + U_{\mathrm{PHS-p}}(\vec{r}_{i,k} - (\vec{R}_j + \vec{u}_j)) \Big], \end{aligned} \tag{5}$$

where $\vec{r}_{i,k}$ denotes the position of the k-th polymer of the i-th particle, and $\vec{u}_i = M(\vec{\Omega}_i)\Delta\vec{u}$ is the vector pointing from the centre of the colloid of the i-th particle to the protrusion, with $M(\vec{\Omega}_i)$ the rotation matrix for the orientation $\vec{\Omega}_i$ of the i-th nanoparticle, and $\Delta\vec{u}$ the vector in the reference frame from the centre of the nanoparticle to the protrusion[6].

Simulation details We employ Monte Carlo (MC) simulations in the canonical NVT ensemble to study the aggregation behaviour of mutually attractive, anisotropic, deformable colloids. We perform two types of simulations: initiating from i) the soluble phase and increasing the interaction strength from $\varepsilon_\mathrm{c} = 3$ to 9 k_BT in steps of 1 k_BT, ii) from a square planar monolayer in a hexagonal packing arrangement with fixed interaction strength $\varepsilon_\mathrm{c} = 9\ k_BT$. We set $N = 98$ and the box length L is set such that the colloid packing fraction equals $\phi_\mathrm{c} = 0.001$; periodic boundary conditions apply in all directions. The protrusions have a radius $r_\mathrm{p} = 0.35\sigma$, they are weakly attractive relative to the colloids: $\varepsilon_\mathrm{p} = \varepsilon_\mathrm{c}/5$, and are randomly oriented below and above the monolayer in system ii. Lastly, the square well width is set to $\Delta = 0.1\sigma$.

We perform 4×10^4 equilibration MC cycles and another 150×10^4 production cycles for each step in system i. Per MC cycle we attempt 50 colloid displacement moves over a fixed maximum distance ($0.25L$), 50 colloid

moves with variable maximum displacement such that $25\% < P_{\text{acc}} < 40\%$, 50 quaternion rotations of the protrusion and another 50 of the entire nanoparticle, 50 cluster moves[30] over a fixed distance ($0.15L$) and $50f/2$ quaternion rotations of polymers. We disable the expensive cluster moves for system ii, allowing us to greatly increase the number of equilibration cycles to 2×10^6 and the number of production cycles to 10×10^6.

For all three systems we perform simulations for every combination of functionality $f \in \{2, 4, 6, 8, 10, 12\}$ and polymer size $q \in \{0.20, 0.25, ..., 0.70\}$, and we repeat all simulations in the absence of protrusions. We repeat the simulations initiated from the hexagonal monolayer an additional four times, and all resulting data plots and morphologies are averages over these runs.

Simulation data analysis We evaluate the average number of bonds per particle using the expression

$$\langle N_{\text{b}} \rangle = \frac{1}{N} \sum_{i \neq j}^{N} \theta(\sigma + \Delta - r_{ij}), \tag{6}$$

where θ is the Heaviside step function. Here, particles are in contact when the centre-centre distance $r_{ij} = |\vec{r}_i - \vec{r}_j|$ between their bodies is less than $\sigma + \Delta$.

We define the covered surface fraction as the surface which is covered by surface groups divided by the total available surface,

$$Q \equiv \frac{f A_q}{A_{\text{tot}} - A_{\text{ex}}}, \tag{7}$$

where A_q is the surface area covered by a satellite sphere, $A_{\text{tot}} = 4\pi((\sigma + \sigma q)/2)^2$ is the total area of the sphere over which the satellite spheres move, and A_{ex} is the surface area excluded by the presence of the protrusion.

A_q and A_{ex} are the curved surface areas of spherical caps. These areas are given by $A_{\text{cap}} = 2\pi R_{\text{cap}} h_{\text{cap}}$, with R_{cap} the radius of the sphere, and $h_{\text{cap}} = R_{\text{cap}} - R_{\text{cap}} \cos\theta_{\text{cap}}$ the height of the cap. In the last equation, θ_{cap} is the angle between the edge of the cap, the centre of the sphere and the centre of the cap. Inserting this in the equation for A_{cap} gives,

$$A_{cap} = 2\pi R_{\text{cap}}^2 (1 - \cos\theta_{\text{cap}}). \tag{8}$$

For the satellite spheres, $R_{\text{cap}} = (\sigma + \sigma q)/2$ and the law of cosines gives,

$$\cos\theta_{\text{cap}} = \frac{(\frac{\sigma+q\sigma}{2})^2 + (\frac{\sigma+q\sigma}{2})^2 - (\frac{q\sigma}{2})^2}{2(\frac{\sigma+q\sigma}{2})(\frac{\sigma+q\sigma}{2})} = 1 - \frac{q^2}{2(1+q)^2}, \tag{9}$$

and for the excluded surface area, $R_{\text{cap}} = (\sigma + \sigma q)/2$ and,

$$\cos\theta_{\text{cap}} = \frac{(\frac{\sigma}{2})^2 + (\frac{\sigma+q\sigma}{2})^2 - (\frac{p\sigma+q\sigma}{2})^2}{2(\frac{\sigma}{2})(\frac{\sigma+q\sigma}{2})} = 1 - \frac{2pq + p^2}{2 + 2q}, \tag{10}$$

with $p = 2r_p/\sigma$, the dimensionless protrusion diameter.

Inserting Eq. 8–10 in Eq. 7 gives,

$$Q = \frac{fq^2}{(1+q)(4+4q-2pq-p^2)}. \tag{11}$$

For particles without protrusions, $p = 0$, this reduces to,

$$Q = \frac{fq^2}{4(1+q)^2}. \tag{12}$$

References

28. van Ravensteijn, B. G. P., Kamp, M., van Blaaderen, A. & Kegel, W. K. General Route toward Chemically Anisotropic Colloids. Chem. Mater. **25**, 4348–4353 (2013). URL `http://dx.doi.org/10.1021/cm4025606`.

29. Asakura, S. & Oosawa, F. On interaction between two bodies immersed in a solution of macromolecules. J. Chem. Phys. **22**, 1255 (1954). URL `http://dx.doi.org/10.1063/1.1740347`.

30. Bhattacharyay, A. & Troisi, A. Self-assembly of sparsely distributed molecules: an efficient cluster algorithm. Chem. Phys. Lett. **458**, 210–213 (2008). URL `http://dx.doi.org/10.1016/j.cplett.2008.04.052`.

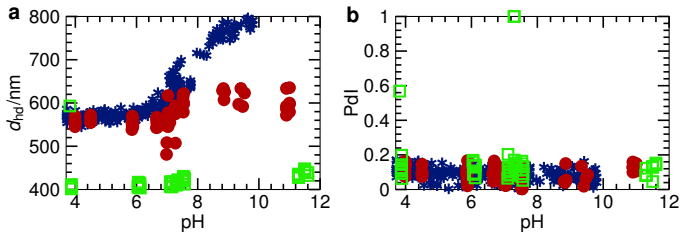

Extended Data Figure 1: *pH-induced structural rearrangements.* For poly(styrene-*co*-acrylic acid) spheres with a transmission electron microscopy diameter, $d = 0.530 \pm 0.014$ µm, the apparent hydrodynamic diameter, d_{hd}, is measured using dynamic light scattering (a). At ionic strength $I \approx 1$ mM, d_{hd} equals 0.79 µm at pH 10, but decreases to 0.57 µm at pH 3 (blue). Upon screening electrostatic interactions at $I \approx 10$ mM (red), or for polystyrene spheres without acrylic acid (green), however, the measured diameter remains almost constant with pH. We conclude that at high pH, electrostatic repulsion between acrylic acid groups triggers the poly(acrylic acid)-rich brush to expand about 0.1 µm into the solution. The measured polydispersity index, PdI, stays constants (b), indicating that changing the pH does not induce aggregation.

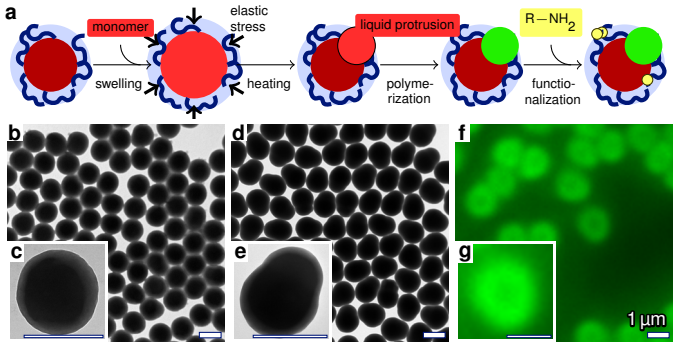

Extended Data Figure 2: *Synthesis.* Schematic outline (a) and microscopy images (b–g) of the synthesis of mutually attractive, anisotropic, deformable particles. Poly(styrene-*co*-acrylic acid) spheres (b–c, transmission electron microscopy) with a hydrophobic core (a, red) and a deformable brush (a, blue) are swollen with monomer, heated, and polymerized, resulting in snowman-like particles (d–e, transmission electron microscopy) with a deformable lobe and a rigid protrusion (a, green). Hydrophobic molecules (a, yellow) are covalently linked to the acrylic acid groups, resulting in fluorescent particles when fluoresceinamine is used (f–g, fluorescence microscopy).

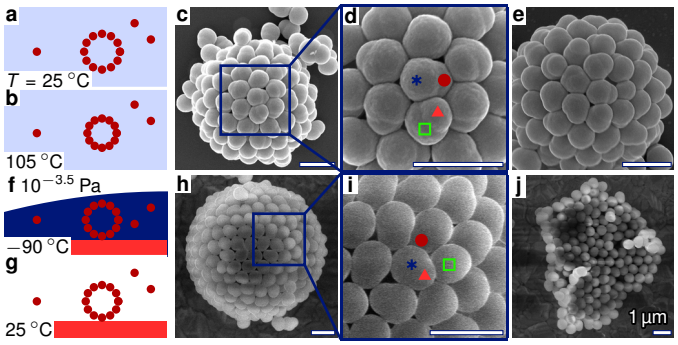

Extended Data Figure 3: *Scanning electron microscopy images of self-assembled microcapsules.* To prevent disintegration upon drying, microcapsules are studied after sintering (a–e) or freeze-drying (f–j). During sintering, the solvent (light blue) is heated in order to partly merge the particles (red) (a–b). During freeze-drying, vitrified water (dark blue) is sublimated under vacuum (f–g). Particles in the microcapsules have six (d,i blue) or five (green) neighbours, and both protrusions that point slightly inwards (red) and outwards (light red) are found. Besides microcapsules, also planar monolayers (j) are observed.

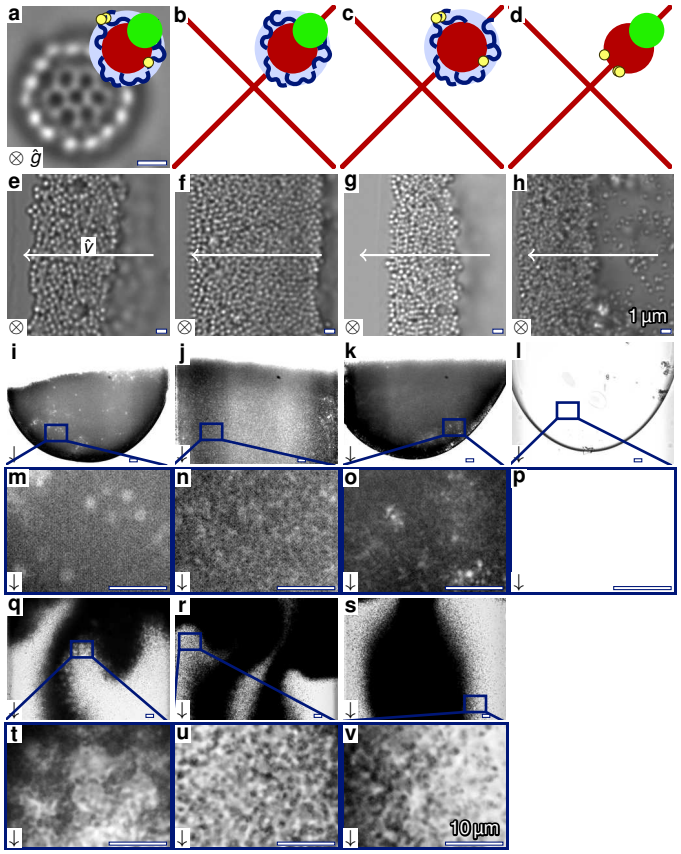

Extended Data Figure 4: *Formation of microcapsules and cavities upon varying the complexity of the particles.* The complexity of mutually attractive, anisotropic, deformable particles (a) that are deformable (blue), anisotropic (green) and functionalized with mutually attractive groups (yellow) is varied resulting in non-functionalized particles (b), isotropic particles (c) and non-deformable particles (d). Microcapsules are only found in the first case (a). Furthermore, all particles are studied using bright field microscopy at the edge of an evaporating droplet (e–h), in a sediment after centrifugation (i–p), and upon diluting the sediment (q–v). The entire images of e–h can be found in Extended Data Fig. 6 and magnifications of i–k can be found in Extended Data Fig. 7b–d. The arrows indicate the directions of the particle flow, $\hat{v}$, and the gravitational field $\hat{g}$.

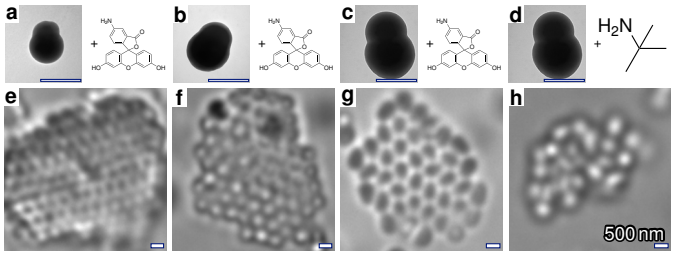

Extended Data Figure 5: *Monolayer sheets.* a) For mutually attractive, anisotropic, deformable particles with varying sizes (a-c), not only hollow microcapsules (Fig. 2), but also two-dimensional hexagonal planar monolayers (e-g) are observed using bright field microscopy. Both fluoresceinamine (a–c,e–g) and *tert*-butylamine (d,h) are used as hydrophobic moieties and for both moieties monolayers are observed.

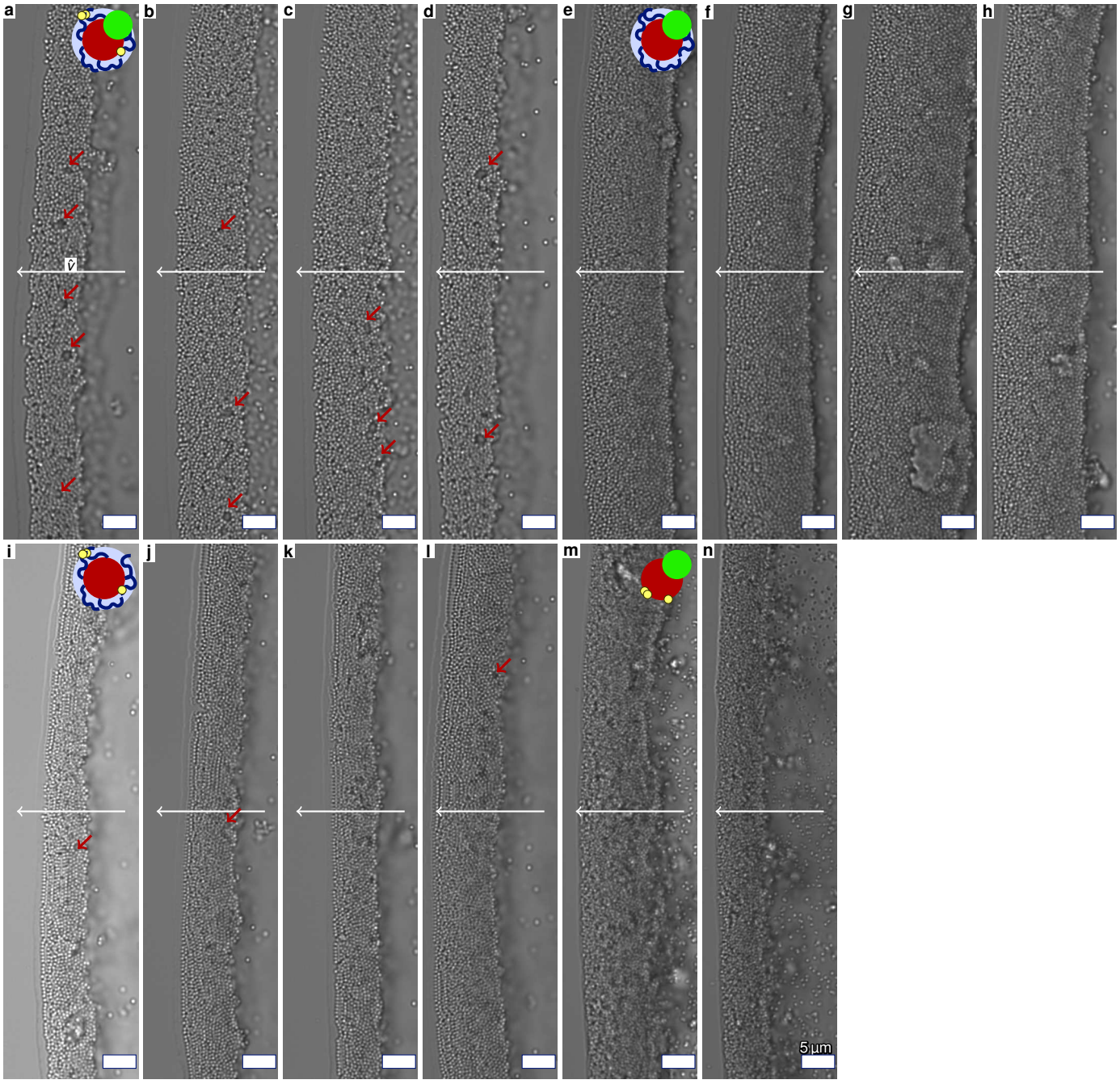

Extended Data Figure 6: *Formation of cavities at the contact line.* The complexity of mutually attractive, anisotropic, deformable particles (a–d) is varied resulting in non-functionalized particles (e–h), isotropic particles (i–l) and non-deformable particles (m–n). For each type, four times (twice for non-deformable particles) a part of the contact line of an evaporating droplet is studied. Many cavities are found for mutually attractive, anisotropic, deformable particles (red arrows), while for isotropic particles much less cavities are found, and the other particles did not show any cavities. Crops of these images can be found in Extended Data Fig. 4. The white arrows indicate the direction of the particle flow, $\hat{v}$.

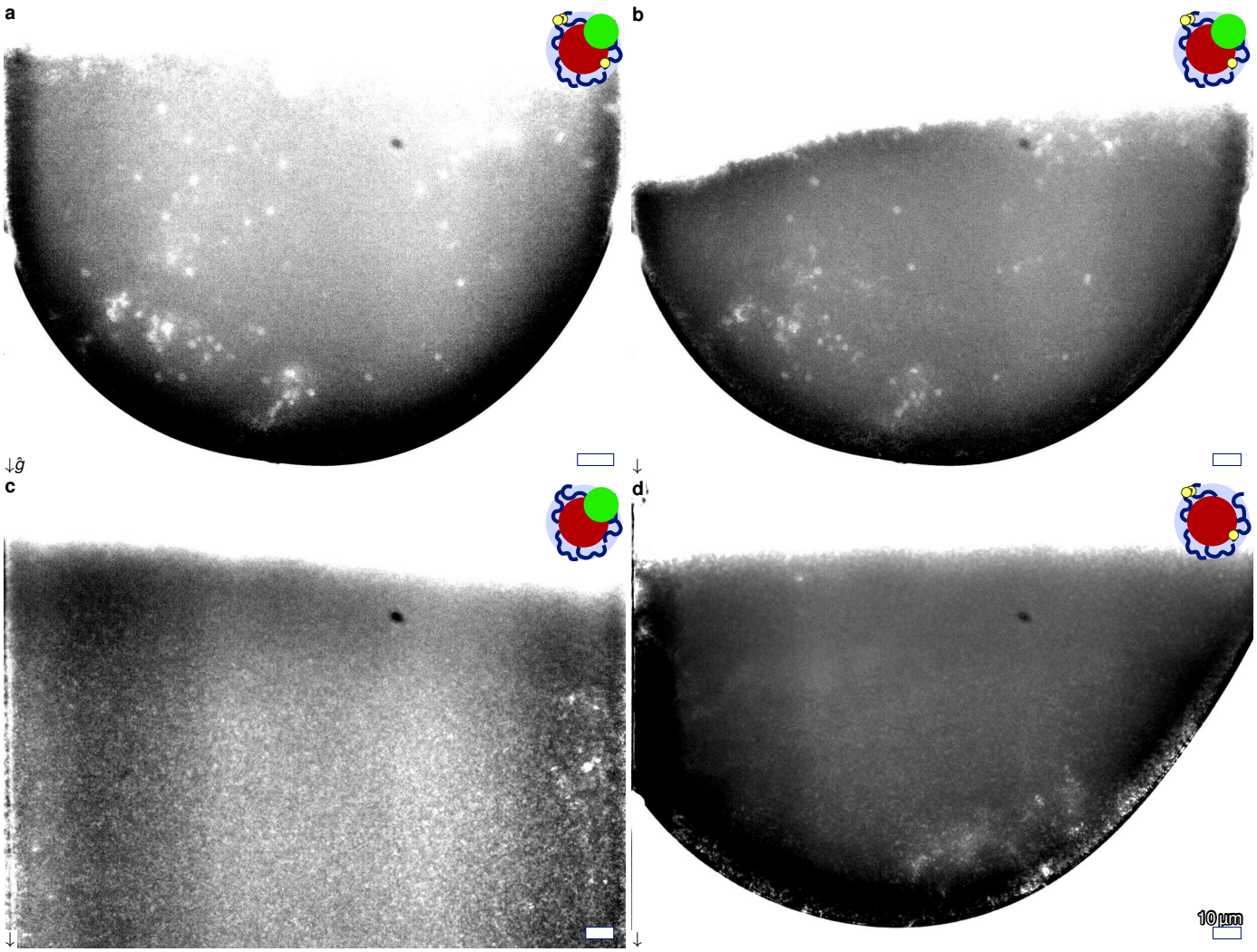

Extended Data Figure 7: *Centrifuged sediments.* Magnifications of the bright field microscopy images Fig. 3r and Extended Data Fig. 4i–k. For mutually attractive, anisotropic, deformable particles, spherical cavities are observed in the sediment (a–b), while the sediments of similar non-functionalized and isotropic particles show no (c) and less (d) cavities.

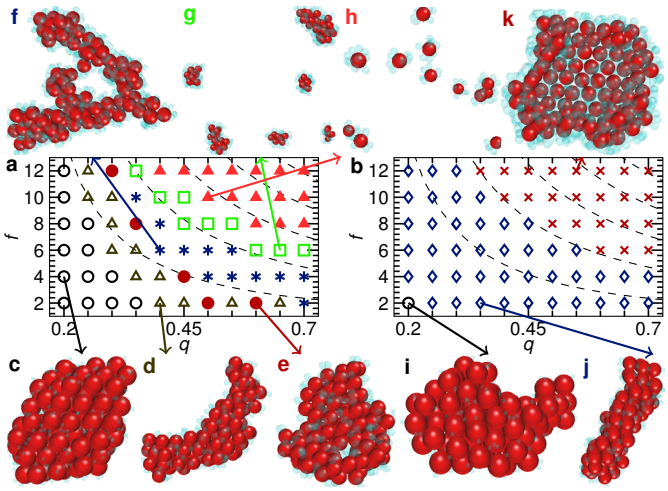

Extended Data Figure 8: *Clusters of isotropic particles.* a-b) Morphology diagrams of mutually attractive, isotropic, deformable particles as a function of the dimensionless diameter of the satellite spheres, q, and the number of satellite spheres, f, and c–k) representative snapshots with cores (red) and satellite spheres (blue). a) When unbound particles are used as the initial configuration and q and f are increased, compact (c, ○), cylindrical (d, △), flattened (e, ●), rod-like (f, ∗) and finite-size (g, □) clusters as well as unbound particles (h, ▲) are found. b) When the initial configuration is a hexagonal monolayer, compact clusters (i, ○), bilayers (j, ◇) and monolayers (k, ×) are observed. The transitions between different morphologies are parallel to isolines for the covered surface fraction, $Q = 0.1$ to 0.5 (dashed).

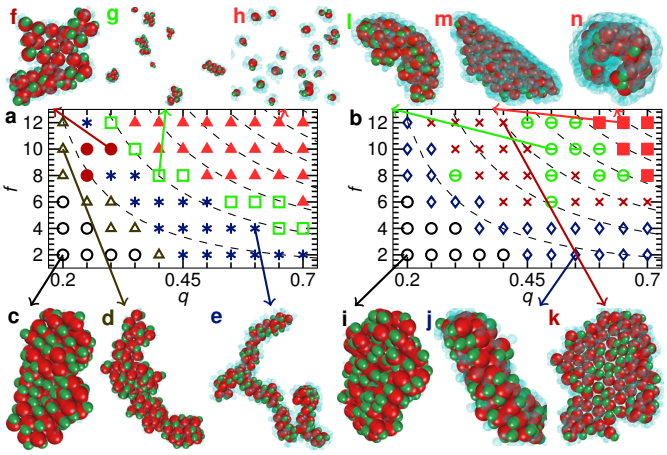

Extended Data Figure 9: *Clusters of anisotropic particles.* a-b) Morphology diagrams of clusters of mutually attractive, anisotropic, deformable particles as a function of the dimensionless diameter of the satellite spheres, q, and the number of satellite spheres, f, and c–n) representative snapshots with cores (red), protrusions (green) and satellite spheres (blue). When unbound particles are used as the initial configuration (a), increasing f and q results in compact (c, ○), cylindrical (d, △), rod-like (e, ∗), flattened (f, ●) and finite-size (g, □) clusters as well as unbound particles (h, ▲). When the initial configuration is a hexagonal monolayer (b), compact clusters (i, ○), bilayers (j, ◇), planar monolayers (k, ×), curved monolayers with in-plane protrusions (l, ⊖) and curved monolayers with out-of-plane protrusions (m–n, ■) are found. The transitions between different morphologies are parallel to isolines for the covered surface fraction, $Q = 0.1$ to 0.7.

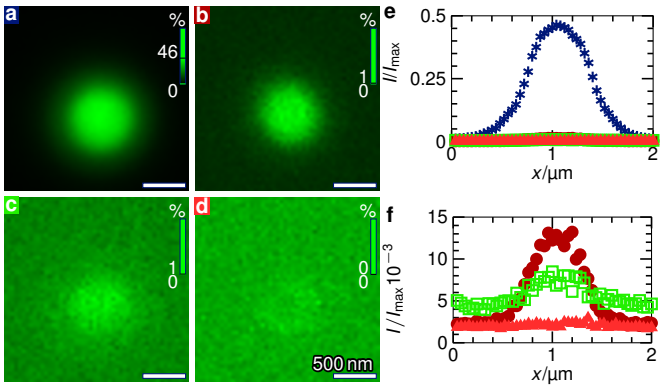

Extended Data Figure 10: *Functionalized CPSAA spheres.* (a-d) Fluorescence microscopy images for variations on the fluoresceinamine coupling method, and (e–f) normalized fluorescence intensity, $I/I_{\max}$, as a function of the distance, x, on the horizontal line through the fluorescence maximum. Poly(styrene-*co*-acrylic acid) spheres activated and functionalized as described in Methods (a,e–f blue). For similarly activated and functionalized polystyrene spheres (b,e–f red). For CPSAA without *N*-(3-Dimethylaminopropyl)-*N*'-ethylcarbodiimide hydrochloride addition (c,e–f green). For CPSAA without fluoresceinamine addition (d,e–f light red). The vertical bars indicate the image level thresholds.